A biomimetic nanocomposite with enzyme-like activities and CXCR4 antagonism efficiently enhances the therapeutic efficacy of acute myeloid leukemia

Fei Kong, Hongliang He, Huiyuan Bai, Fang Yang, Ming Ma [**], Ning Gu [***], Yu Zhang [*]

State Key Laboratory of Bioelectronics, Jiangsu Key Laboratory for Biomaterials and Devices, School of Biological Science and Medical Engineering & Collaborative Innovation Center of Suzhou Nano Science and Technology, Southeast University, Nanjing, 210096, PR China

ARTICLE INFO

ABSTRACT

Despite the progress made to improve therapeutic outcomes for acute myeloid leukemia (AML), many unmet clinical needs remain to be resolved. Unlike existing anti-AML strategies, here we developed a biomimetic nanocomposite to efficiently eliminate the leukemia cells in the bone marrow and prevent the homing of AML. To fulfill our design, the ultra-small nanozyme was conjugated onto the surface of an oxygen-carrying nanoparticle, which was further coated with bone marrow stromal cell membrane. After entering the blood, this biomimetic nanocomposite got actively internalized by the leukemia cells in the blood and released the loaded chemo-therapeutics and nanozyme inside the leukemia cells to achieve a synergistic antitumor efficacy. Meanwhile, the adhesive properties of the stromal cell membrane enabled the nanocomposite to home to the bone marrow, where the nanocomposite effectively killed the retained leukemia cells. More importantly, the biomimetic cell membrane also acted as a CXCR4 antagonism to block the CXCR4/CXCL12-mediated homing of leukemia cells to the bone marrow and infiltration to other organs like the liver and spleen. In conclusion, this proof-of-concept study demonstrated that our designed platform effectively kills leukemia cells while preventing their infiltration, thus providing a promising prospect for resolving the clinical challenges in current AML treatment.

1. Introduction

Acute myeloid leukemia (AML) is a cancer of the bone marrow and the blood and is one of the most common types of leukemia in adults [1, 2]. According to the latest estimates from the United States, the annual incidence of AML is 4.3 per 100,000 worldwide, presenting a steady upward trend yearly [3,4]. The conventional treatments for AML are composed of chemotherapy, radiation therapy, stem cell transplant [5]. Despite some success obtained with conventional treatments, the efficacy of AML treatment remains unsatisfactory in many patients, due to incomplete elimination of leukemia cells, trafficking and infiltration of leukemia cells, and chemoresistance in leukemia cells [4]. Moreover, the toxicity of chemotherapy keeps posing a substantial safety concern in the clinic [6]. Additionally, a large number of leukemia patients experience relapsed leukemia even after successful initial chemotherapy.

Therefore, alternative approaches that can efficiently eliminate residual AML cells in the bone marrow and prevent infiltrative leukemia are highly desirable.

CXCR4 is a seven-transmembrane G-protein-coupled chemokine receptor expressed by hematopoietic cells [7]. Stromal cells in the bone marrow constitutively secrete stromal cell-derived factor-1 (CXCL12), the ligand for CXCR4 [8]. There is also growing evidence suggesting that residual AML cells in the blood will home to the bone marrow and adhere to stromal cells through the CXCR4/CXCL12 axis, which allows for AML cell growth and protect the AML cells from chemotherapy-induced death commonly seen in the treatment of patients with AML [9]. The inhibition of the CXCR4-CXCL12 axis can effectively inhibit the migration and adhesion of AML cells to CXCL12-secreting stromal cells in the marrow [10]. For example, some clinically approved CXCR4 antagonists (Plerixafor and T140 analogs)

can effectively prevent the migration of AML cells by blocking CXCR4 receptors, thus mobilizing AML cells from protective stromal microenvironment marrow and exposing them more accessible to chemo drugs [11]. Therefore, the CXCR4-CXCL12 axis has been increasingly regarded as a promising therapeutic target for the treatment of AML.

Recently, cell membrane-derived biomimetic nanoparticles have emerged as an attractive therapeutic platform. While preserving the inherent physicochemical properties of nanoparticles, camouflaging the nanoparticles with natural cell membranes can enable them to mimic the biological functions of the source cells, improve their pharmacokinetic profiles *in vivo*, and achieve the preferential accumulation in desire tissues similar to the source cells [12,13]. Cell membrane camouflaging nanotechnology has been widely applied in various biomedical applications, including tumor therapy, diagnostic imaging, detoxification, and immuneregulation [12,14–17]. For example, Yan et al. coated nanozymes with the cell membrane and demonstrated that these engineered nanozymes achieved excellent photoacoustic imaging in the treatment of nasopharyngeal carcinoma [18]. Dong et al. constructed leukemia cell membrane-derived nanoparticles (DAazo@CMSN). This biomimetic nanoparticle could effectively target the residual leukemia cells in the bone marrow microenvironment, achieving the precise delivery of both a therapeutic neutralizing antibody and one chemotherapy drug, thus enhancing the effect of chemotherapy [19].

The merits of cell membrane coating nanotechnology inspired us to design these nanocomposites as an anti-leukemia strategy to solve the limitations in current AML treatment. Residual AML cells in the marrow and the ensuing occurrence of drug resistance are mediated by CXCR4-CXCL12 axis-induced leukemia cell trafficking and homing to the marrow microenvironment. Bone marrow stromal cells have been found to overexpress CXCL12 [20,21]. The nanoparticles coated with marrow stromal cell membranes act as an innovative nano CXCR4 antagonist to efficiently target AML cells and then block the CXCR4/CXCL12 interaction, inhibiting the return of leukemia cells to bone marrow, preventing leukemia cells from infiltrating into body tissues, like the liver or spleen.

Nanozymes are nanomaterials with excellent enzyme-mimetic catalytic activity. The progress of nanozymes is expected to provide an impetus for solving clinical problems and developing new therapeutic schemes. For example, Pt nanozyme has been proved that have a variety of oxidoreductase activities, including peroxidase (POD), catalase (CAT), superoxide dismutase (SOD), and oxidase (OXD) [22]. Pt nanozyme can catalyze the conversion of glucose to gluconic acid and H_2O_2 by simulating OXD; it can also act as $O_2\bullet^-$ scavenger to quickly convert harmful $O_2\bullet^-$ into H_2O_2 and O_2 [23]. Under weak acidic pH conditions, Pt nanozyme has the POD activity of catalyzing H_2O_2 to form highly toxic •OH. In addition, the CAT activity of Pt nanozyme was demonstrated by decomposing H_2O_2 into non-toxic H_2O and O_2 under neutral pH conditions [24]. Nanozymes-based chemodynamic therapy is an emerging form of nanocatalytic tumor therapy, which uses catalytic reactions induced by nanozymes to convert endogenous chemicals (such as H_2O_2) overexpressed in tumors into reactive oxygen species (ROS) to destroy cancer cells. Since it has few side effects and does not require exogenous energy, becomes an effective cancer treatment strategy. Nanozymes can also reduce multidrug resistance in cells to achieve the best therapeutic effects. Qian et al. developed ROS-responsive platinum nanozyme polymer nanoparticles that can effectively catalyze the decomposition of hydrogen peroxide (H_2O_2) into oxygen to alleviate hypoxia and further enhance the photodynamic chemotherapy of colon cancer [25].

Herein, we utilized the cell membrane coating technology to construct a biomimetic nanocomposite for improved anti-leukemia efficacy. First, to achieve better catalytic properties, an optimal version of Pt nanozyme was prepared by loading perfluorobromooctane (PFOB) and Pt nanozyme into PLGA nanospheres (PFOB@PLGA@Pt). Mouse bone marrow stromal cell membrane (MS-5 cell) was used as the coating materials to modify the PFOB@PLGA@Pt core. To achieve synergistic

chemotoxicity, doxorubicin was loaded into the MS-5 cell membrane. The resulting mediated biomimetic nanocomposite that can mimic the bone marrow stromal cells and home to bone marrow circulated in the blood for a longer time, efficiently blocked the trafficking of AML cells to the bone marrow through the CXCR4-CXCL12 axis, and meanwhile kill AML cells via the pro-apoptotic properties of nanozyme and DOX (Scheme 1).

2. Results and discussion

### 2.1. Synthesis and characterization of biomimetic nanocomposite

The detailed fabrication process of the PFOB@PLGA@Pt@DOX-CM biomimetic nanocomposite was illustrated in Scheme 1. Briefly, the perfluorobromooctane (PFOB) as the oxygen supply core was first encapsulated into a biocompatible polymer PLGA (PFOB@PLGA). After that, the surface of PFOB@PLGA was conjugated by multiple ultra-small Pt nanoparticles with enzymatic activities to form PFOB@PLGA@Pt. Finally, the PFOB@PLGA@Pt@DOX-CM was constructed by wrapping PFOB@PLGA@Pt in MS-5 cell membranes containing chemotherapy drugs of DOX. The morphology of different nanoparticles was visualized by high-resolution transmission electron microscopy (HR-TEM). As shown in Fig. 1b, there was many Pt nanoclusters deposited on the surface of PLGA nanospheres. A clear core-shell structure in the PFOB@PLGA@Pt surface was observed, consistent with the previous reports using a unilamellar membrane coating around the polymeric nanoparticle core (Fig. 1c) [18]. Dynamic light scattering (DLS) data as shown in Fig. 1d revealed that PFOB@PLGA@Pt presented a spherical particle with ~114 ± 12 nm diameter, which was slightly increased to ~125 ± 14 nm when covered by cell membranes. In addition, the zeta potential of PFOB@PLGA@Pt was −12 ± 4 mV and decreased to −21 ± 5 mV after cell membranes coating (Fig. 1e). As further confirmed by elemental mapping analysis (Fig. 1a and b and Fig. S1a), typical F, Br, Pt distributions in the PFOB@PLGA@Pt suggested that the successful PFOB entrapment in PLGA nanoparticle core and the attachment of Pt onto the surface of PLGA nanoparticle. Taken together, these results demonstrated that the successful fabrication of PFOB@PLGA@Pt@CM nanocomposites, providing an opportunity for cascading catalytic reaction-based AML therapy.

To further determine the CXCR4 antagonistic functions of the MS-5 cell membrane, the CXCL12 expression levels in MS-5 cells, MS-5 cells membrane-derived vesicles, and PFOB@PLGA@Pt@DOX-CM nanocomposites were studied using Western blot analysis [20,26]. As shown in Fig. 1f, the results suggested that MS-5 cells, MS-5 cells membrane-derived vesicles, and PFOB@PLGA@Pt@DOX-CM nanocomposites maintained critical cytokine CXCL12, the ligand for CXCR4.

2.2. The enzymatic activities of biomimetic nanocomposite

Based on the successful fabrication of biomimetic nanocomposite, the oxygen-carrying capacity and enzyme catalytic ability of biomimetic nanocomposites were thoroughly evaluated. Ultrasonic images were captured at 0, 5, and 10 min after the injection of nanocomposites into the volume model pipeline. The results were shown in Fig. 2a, compared with the PLGA loaded with soybean oil (PLGA@SO) as the control, the number of oxygen bubbles in PFOB@PLGA ultrasonic images got increased, and the most significant oxygen bubble generation in PFOB@PLGA@Pt was observed. The ultrasonic effect of PFOB@PLGA@Pt could maintain for at least 10 min, indicating that PFOB@PLGA@Pt possessed a strong oxygen-carrying function.

The peroxidase-like activity of different nanocomposites was also evaluated by catalytic oxidation of 3,3′,5,5′-Tetramethylbenzidine (TMB) substrate in the presence of H_2O_2. As illustrated in Fig. S1b, PLGA@Pt and PFOB@PLGA@Pt rapidly catalyzed the oxidation of TMB to produce blue oxidation products with the highest absorbance at 652 nm. By contrast, the same concentration of PFOB@PLGA did not cause a
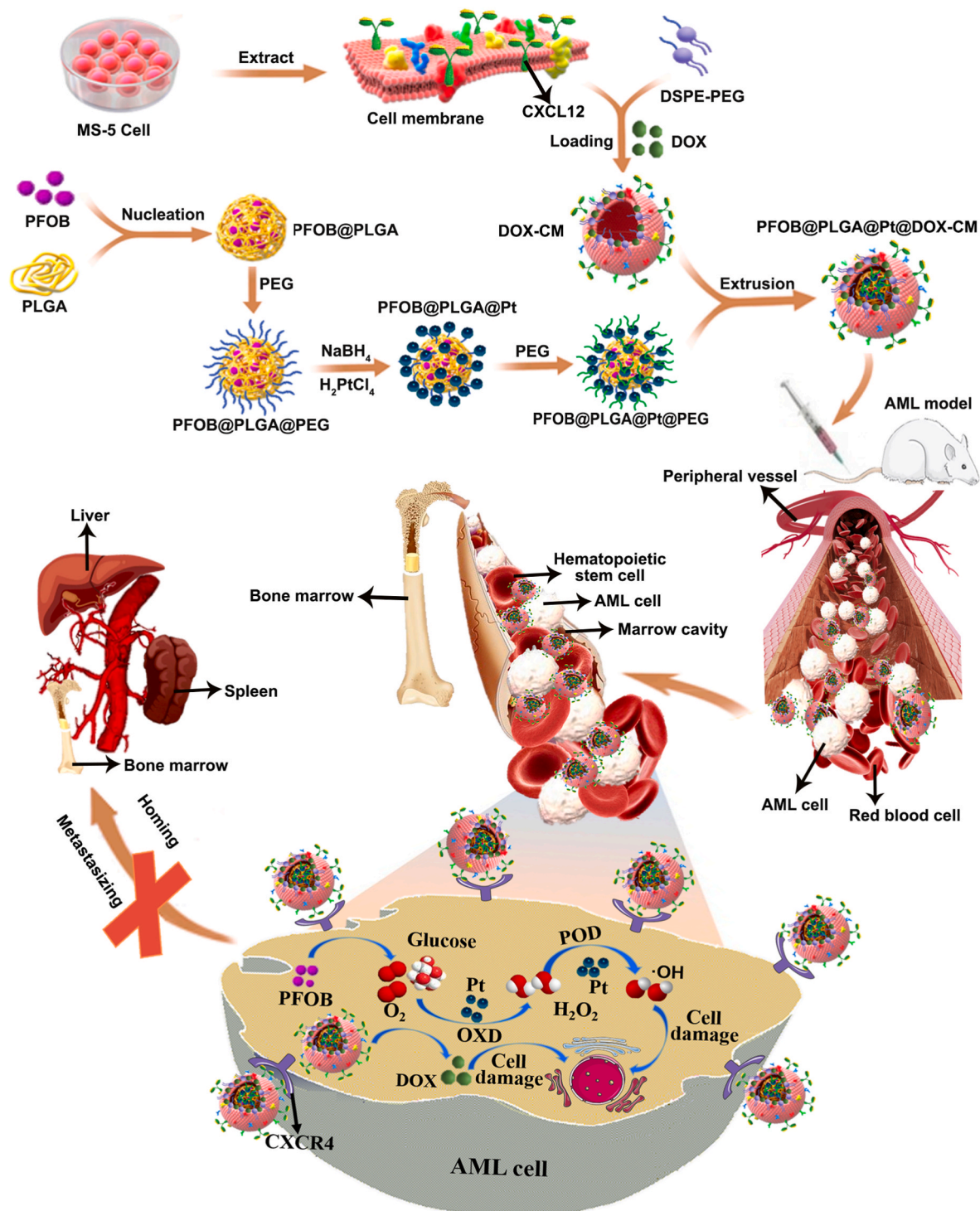
Scheme 1. Schematic illustration of biomimetic nanocomposites designed for enhancing anti-leukemia efficacy. Through the CXCR4-CXCL12 axis, the PFOB@PLGA@Pt@DOX-CM binds to the leukemia cells in the blood, where released PFOB, DOX, and Pt in AML cells. The PFOB@PLGA@Pt@DOX-CM generated chemotoxicity and excessive ROS resulted from Pt nanozyme to induce leukemia cell apoptosis. Moreover, bone marrow stromal cell membrane coating enabled the PFOB@PLGA@Pt@DOX-CM to home to the bone marrow, where acted as CXCR4 antagonists to block the leukemia cell-stroma adhesive interactions, thus making AML cells better accessible to conventional therapies, inhibiting the growth of residual AML cells in the bone marrow, and preventing the infiltration of AML cells to other normal organs, like the liver and spleen.

color change in TMB. Compared with other groups, PFOB@PLGA@Pt revealed the highest catalytic efficiency for TMB oxidation. To quantify the catalytic efficiency of PFOB@PLGA@Pt, typical Michaelis-Menten curves of nanocomposites were obtained to study the effects of both TMB and H_2O_2 concentrations on the catalytic rate (Fig. 2b). In short, the catalytic rate of nanocomposites enhanced along with the increase of

TMB or H_2O_2 in a certain concentration range. Steady-state dynamics parameters were calculated according to the Michaelis-Menten equation as shown in Table S1, where the maximum initial velocity (V_{max}) of PFOB@PLGA@Pt was 0.39 μMs^{-1} and the Michaelis constant (K_m) was 0.12 mM. Furthermore, it can be seen from the catalytic constant (K_{cat}) that the catalytic efficiency of PFOB@PLGA@Pt was greater than
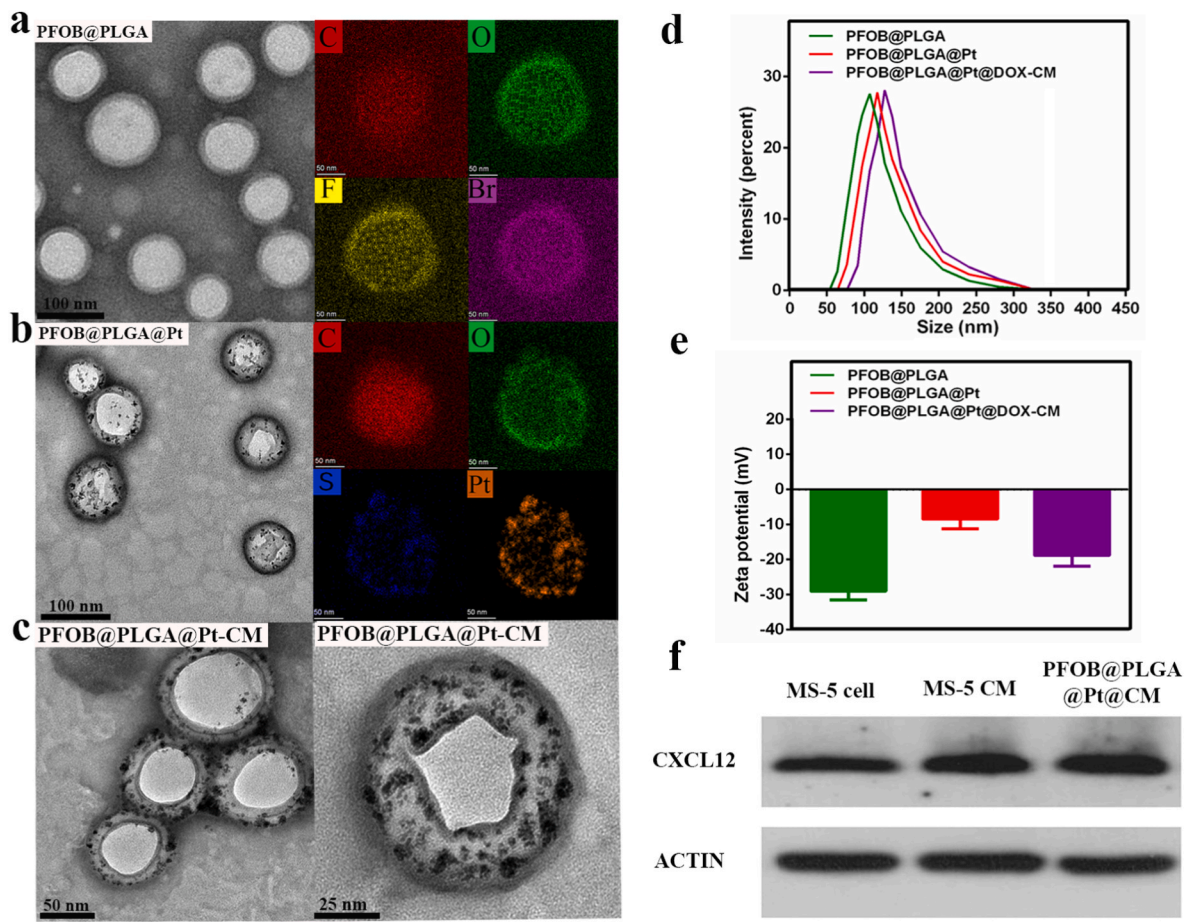
Fig. 1. Representative TEM images of the nanocomposites in each synthetic stage. (a) Images of PFOB@PLGA stained with phosphotungstic acid and corresponding EDS element mappings images. (b) Images of PFOB@PLGA@Pt stained with phosphotungstic acid and element mapping images. (c) Images of PFOB@PLGA@Pt@CM stained with phosphotungstic acid. (d) Hydrodynamic size of nanocomposites in each step during the fabrication of PFOB@PLGA@Pt@DOX-CM. (e) ζ potential change of nanocomposites in each step during the fabrication of PFOB@PLGA@Pt@CM. (f) Western blot analysis of CXCL12 expression in MS-5 cells, MS-5 cells membrane vesicles, and PFOB@PLGA@Pt@DOX-CM nanocomposite.
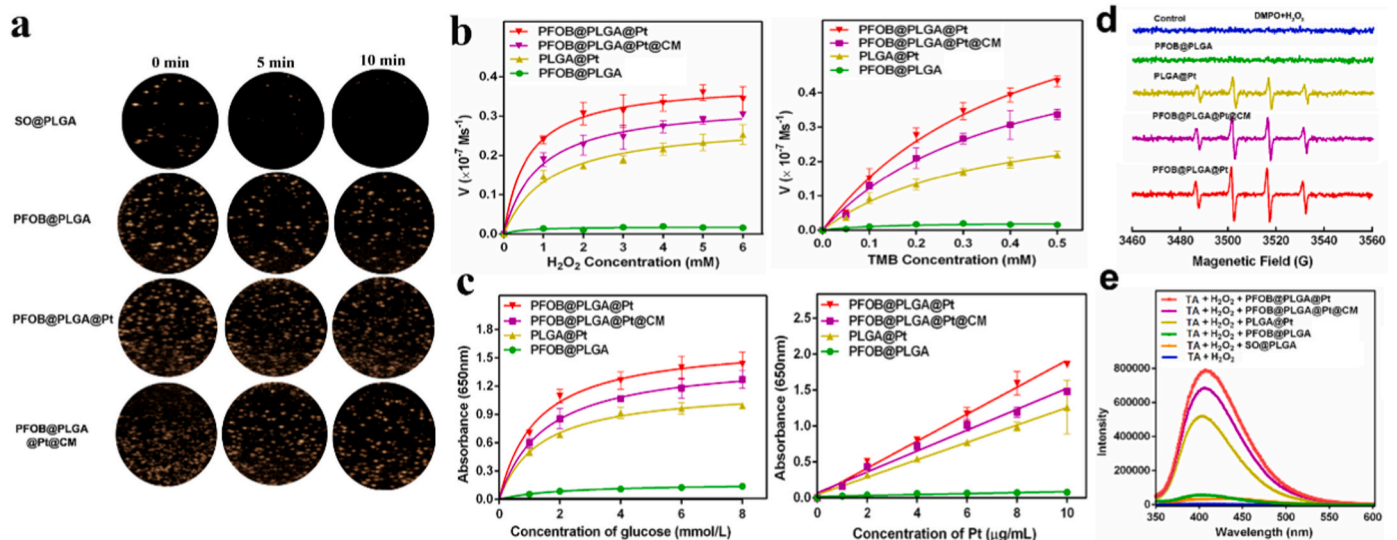

Fig. 2. Oxygen carrying capacity and enzyme-like properties of nanocomposites. (a) The oxygen-carrying capacity of nanocomposites was detected by ultrasonic imaging. (b) The velocity of the catalytic reaction was measured using different concentrations of H_2O_2 (0–6 mM) and TMB (0–0.5 mM) at room temperature. (c) The glucose oxidase activity of biomimetic nanocomposites was explored by a two-step method. (d) ESR spectra of BMPO/·OH adducts were obtained from samples containing 0.2 M nanocomposites, 1×10^{-3} M H_2O_2 and 0.05 M DMPO. (e) Fluorescence spectra were obtained from different reaction systems to detect the formation of •OH.

PLGA@Pt. The results indicated that the oxygen-involved oxidase activity promoted the peroxidase activity of Pt, while the peroxidase-like activity of the membrane modified Pt was decreased, which was largely due to restricted substrate diffusion by the surface coating.

Biomimetic nanocomposites can oxidize glucose to produce gluconic acid and H_2O_2, formed H_2O_2 further oxidizes TMB. Therefore, a two-step method was used to explore the glucose oxidase activity of biomimetic nanocomposites. The glucose oxidase activity of biomimetic nanocomposites has a linear relationship with the concentration of glucose and the concentration of biomimetic nanocomposites and is highly sensitive to glucose (Fig. 2c). Superior characteristics of glucose oxidase are beneficial to bionic nanocomposites to consume a large amount of endogenous glucose in tumor cells to play a role in starvation treatment. It is further proved that biomimetic nanocomposites possess the ability of cascade catalysis.

The peroxidase-like activity mechanism of PFOB@PLGA@Pt@DOX-CM nanocomposites may result from the catalytic decomposition of H_2O_2 into •OH. Therefore, the trapping agent of 5,5-dimethyl-1-pyrroline N-oxide (DMPO) was utilized to directly capture this short-lived hydroxyl radical (•OH) to detect the generation of •OH by electron spin resonance (ESR) [27], the ESR spectra of samples were shown in Fig. 2d. The characteristic ESR signal of DMPO/•OH was negligible in the presence of PFOB@PLGA. In contrast, a strong ESR spectrum with 1:2:2:1 lines appeared upon the addition of PLGA@Pt, PFOB@PLGA@Pt@CM, PFOB@PLGA@Pt. Moreover, the ESR signal strength of PFOB@PLGA@Pt was stronger than that of PLGA@Pt alone. Hence, these results clearly showed that the peroxidase-like activity of PFOB@PLGA@Pt was the result of the catalytic decomposition of H_2O_2 to generate •OH. Interestingly, since PFOB improved the catalytic activity of Pt nanozyme, •OH produced by PFOB@PLGA@Pt was higher than that of PLGA@Pt alone. In addition to ESR, terephthalic acid (TA) was also commonly utilized as it can easily react with •OH to generate 2-hydroxy terephthalic acid (TAOH) with a unique fluorescence signal at 435 nm [28,29]. Fig. 2e showed the fluorescence spectra before and after the addition of nanocomposites. H_2O_2 itself has no fluorescent signal at excitation wavelengths of 385 nm. When PLGA@Pt and
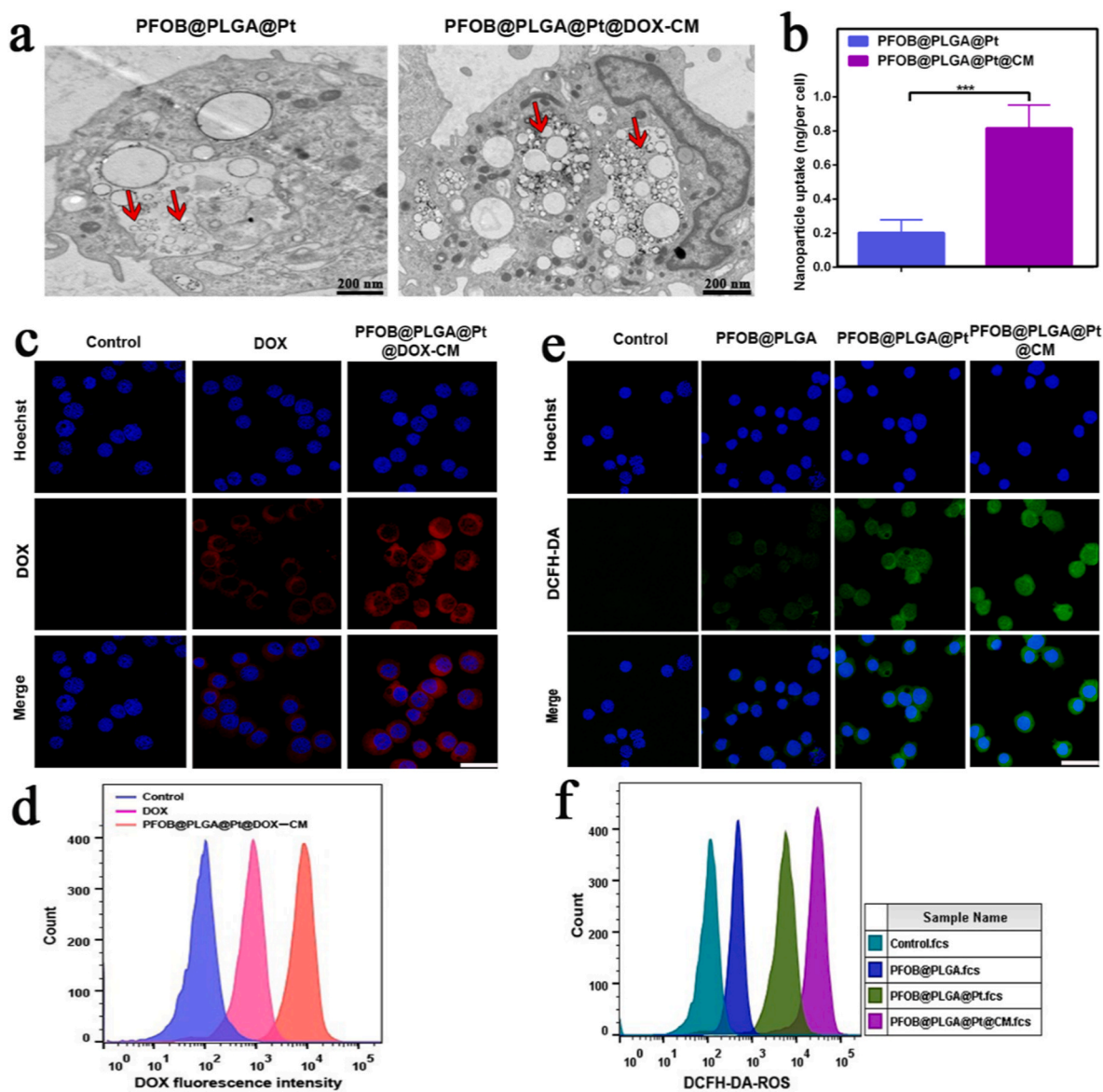

Fig. 3. (a) Visualization of HL-60 cells treated with PFOB@PLGA@Pt@DOX-CM and PFOB@PLGA@Pt for 10 h using TEM, the red arrow refers to the nanocomposites entering the lysosome. (b) The cellular uptake of Pt ions was quantitatively measured by ICP-MS. (c) CLSM images of HL-60 cells upon incubation with free DOX, PFOB@PLGA@Pt@DOX-CM for 10 h, scale bar: 30 μm. (d) DOX uptake in HL-60 cells was detected by flow cytometry. (f) Flow cytometry analysis of ROS generation in HL-60 cells treated with different nanocomposites using DCFH-DA probes.

PFOB@PLGA@Pt were added, strong fluorescence signals appeared with an emission peak at 435 nm, while negligible fluorescence signal was observed in the PFOB@PLGA group. Hence, the above results demonstrated that PFOB@PLGA@Pt possessed excellent peroxidase-like activity to generate •OH during the decomposition of H_2O_2.

2.3. Cellular uptake of biomimetic nanocomposites

Afterward, the cellular uptake of biomimetic nanocomposites on HL-60 cells was also observed by Bio-TEM and quantified by ICP-MS. As shown in Fig. 3a, PFOB@PLGA@Pt@DOX-CM nanocomposites were easily internalized into lysosomes after 10 h co-culture, which is conducive to exert pro-oxidation ability of nanocomposites under acid conditions. Comparatively, the cellular uptake amount of PFOB@PLGA@Pt@DOX-CM was far more than that of PFOB@PL-GA@Pt, indicating that cell membrane carriers promote cellular absorption of nanocomposites (Fig. 3b). Then the cellular drug uptake was further examined by flow cytometry and CLSM. As illustrated in Fig. 3c and d, obvious red fluorescence inside the cytoplasm of cells treated with PFOB@PLGA@Pt@DOX-CM was observed. Only faint red fluorescence in the cytoplasm of DOX-treated cells was observed. These observations suggested that the modification of cell membrane was beneficial to the internalization of PFOB@PLGA@Pt@DOX-CM into HL-60 cells, leading to effective cellular accumulation of the drug.

2.4. Biomimetic nanocomposites induced intracellular ROS generation

Dichlorofluorescein diacetate (DCFH-DA) was used as a fluorescent indicator for reactive oxygen species (ROS) in cells using flow cytometry

and CLSM. The green fluorescence intensity of DCFH-DA was indicative of the intracellular ROS generation. As shown in Fig. 3f, PFOB@PLGA displayed very weak fluorescence signals, while PFOB@PLGA@Pt showed strong fluorescence signals. Among them, the fluorescence signal intensity in HL-60 cells treated with the PFOB@PLGA@Pt@CM was significantly higher than other groups, indicating that the intracellular ROS generation of PFOB@PLGA@Pt@CM was better than the others. The fluorescent images were presented in Fig. 3e, the PFOB@PLGA-treated cells displayed weak green fluorescence, but bright green fluorescence could be observed in PFOB@PLGA@Pt and PFOB@PLGA@Pt@CM-treated cells, especially. These results suggested that both Pt nanozyme loading and cell membrane modification mainly contributed to ROS generation.

2.5. Drug loading and release in vitro

Next, the loading content and encapsulation efficiency of DOX were calculated according to the standard curve of DOX. It was found that DOX loading content and encapsulation efficiencies were $9.4 \pm 3.5\%$ and $73.2 \pm 2.5\%$, respectively, which suggested that cell membranes possess a high drug loading rate. The release behavior of DOX and Pt ions from PFOB@PLGA@Pt@DOX-CM under extracellular physiological conditions was evaluated. As displayed in Fig. 4a, the total release of DOX and Pt ions reached $80 \pm 5\%$ and $12 \pm 3\%$ at the end of the test (120 h) in PBS solution (pH = 7.4), respectively. Compared with neutral pH conditions, the drug release rate of DOX ($85 \pm 4\%$) and Pt ions ($18 \pm 3\%$) were slightly enhanced under weak acidic conditions (pH = 4.5), mainly because of the degradation of membrane and the protonation of DOX under a weak acid condition. Therefore, it was concluded that DOX
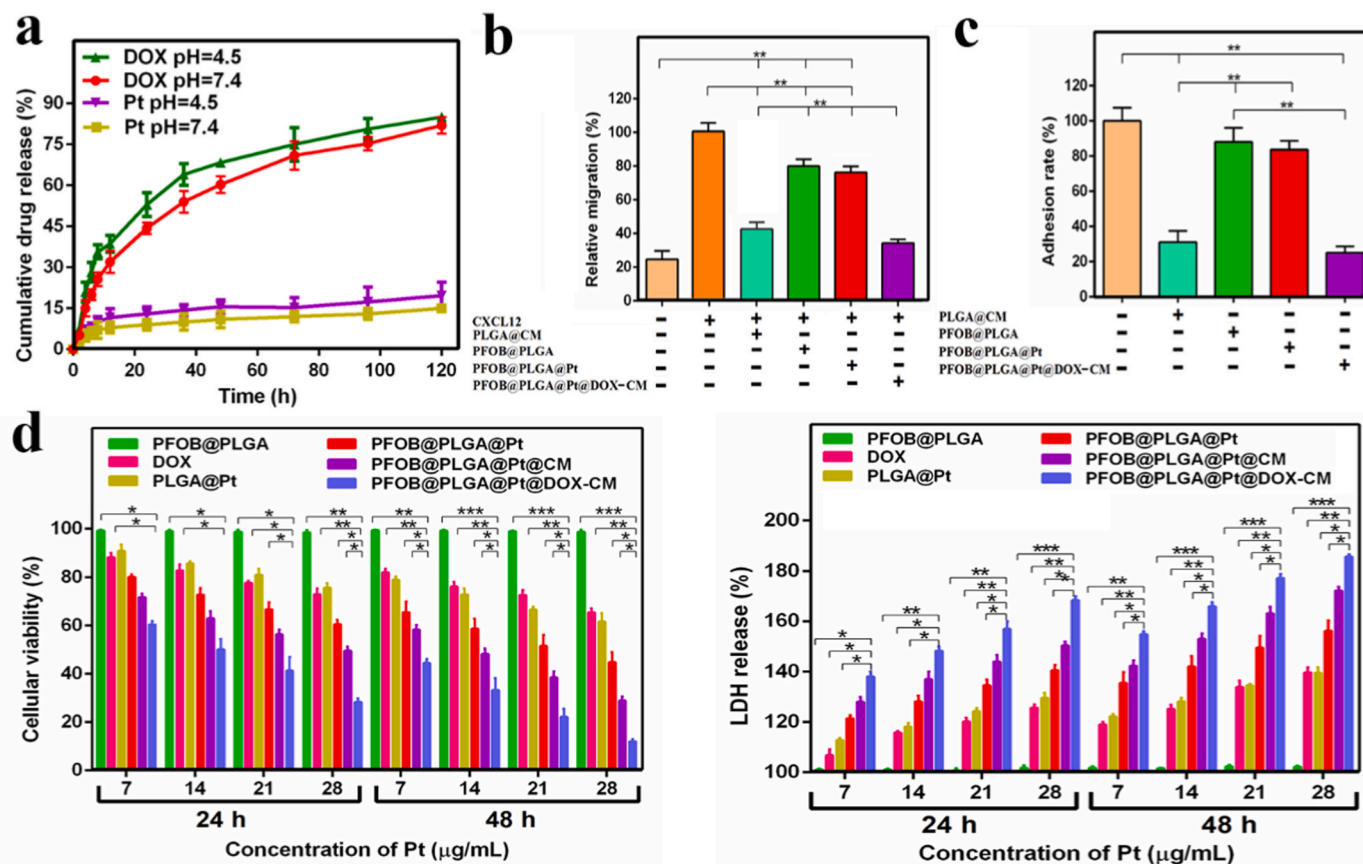

Fig. 4. Anti-AML effect of biomimetic nanocomposites *in vitro*. (a) *In vitro* release curve of DOX and Pt from PFOB@PLGA@Pt@DOX-CM. (b) Inhibitory effect of PFOB@PLGA@Pt@DOX-CM on CXCL12-induced HL-60 cells migration (*P < 0.05, **P < 0.01, ***P < 0.001, n = 3). (c) Inhibitory effect of PFOB@PLGA@Pt@DOX-CM on HL-60 cells adhesion to MS-5 cells (*P < 0.05, **P < 0.01, ***P < 0.001, n = 3). (d) Cell viability of HL-60 cells treated with different concentrations of nanocomposites for 24 h and 48 h (*P < 0.05, **P < 0.01, ***P < 0.001, n = 5).

was slowly released from biomimetic nanocomposites at the extracellular level, which contributes to effective drug delivery for AML therapy.

2.6. Inhibitory effect of nanocomposites on migration and adhesion of HL-60 cells in vitro

The migration and adhesion behavior of HL-60 cells were studied by the transwell method. CXCL12 was applied to mimic the bone marrow microenvironment *in vitro*. HL-60 cells were pretreated with different nanocomposites for 2 h and then inoculated into the upper compartment of transwell equipment. A culture medium containing a certain concentration of CXCL12 (100 ng/mL) was directly added into the lower compartment of the transwell device. As shown in Fig. 4b, the relative mobility of HL-60 cells was low ($22 \pm 3.0\%$) when CXCL12 was not supplied in the transwell's bottom compartment. However, the migration ability of HL-60 cells significantly enhanced in the existence of CXCL12 in the bottom compartment medium (set as control, the relative mobility is measured at 100%). But, when HL-60 cells were pretreated with PLGA@CM, PFOB@PLGA, PFOB@PLGA@Pt, and PFOB@PLGA@Pt@DOX-CM, the migration of HL-60 cells decreased to $40 \pm 4.5\%$, $87 \pm 3.6\%$, $83 \pm 5.2\%$, $31 \pm 2.8\%$, respectively. Notably, the migration rate of HL-60 cells pretreated with cell membrane-coated nanocomposites was lower than that with PFOB@PLGA@Pt and PFOB@PLGA, suggesting that cell membrane-coated nanocomposites availably inhibited the CXCL12-mediated migration of HL-60 cells. MS-5 cells provide clonal substitutes for bone marrow matrix niches and can continuously secret CXCL12. Besides, the CXCL12 secretion of MS-5 cells was similar to that of human bone marrow stromal cells [7,30]. Therefore, MS-5 cells were used to further evaluate whether biomimetic nanocomposites interfere with the adhesion of HL-60 cells to the bone marrow microenvironment (Fig. 4c). As expected, the adhesion rate of PLGA@CM ($36 \pm 4.3\%$) and PFOB@PLGA@Pt@DOX-CM ($30 \pm 3.5\%$) on HL-60 cells were stronger in comparison with PFOB@PLGA ($90 \pm 3.3\%$) and PFOB@PLGA@Pt ($85 \pm 5.0\%$). These results revealed that PFOB@PLGA@Pt@DOX-CM efficiently blocked CXCL12-induced migration and adhesion of HL-60 cells to bone marrow.

2.7. In vitro anti-AML activity of biomimetic nanocomposites

Then, the *in vitro* cytotoxicity of biomimetic nanocomposites was evaluated by classical CCK-8 and LDH assay using the multimode reader. The viability of HL-60 cells after 24 h and 48 h treatment with free DOX and nanocomposites was examined. As illustrated in Fig. 4d, Dox and nanocomposites revealed a dose-dependent inhibitory effect on the proliferation of HL-60 cells. After exposure for 48 h, the cell viability of PBS treatment group was set to 100%, whereas the cell viability induced by free DOX, PLGA@Pt, PFOB@PLGA@Pt, PFOB@PLGA@Pt@CM, PFOB@PLGA@Pt@DOX-CM (PFOB concentration of 7 μg/mL, DOX concentration of 25 μg/mL, Pt concentration of 28 μg/mL) was $65.2 \pm 4.2\%$, $61.3 \pm 4.1\%$, $44 \pm 3.3\%$, $28.2 \pm 3.8\%$, and $12.7 \pm 2.6\%$, respectively. The modification of the cell membrane made the nanocomposites more efficiently enter cells and carry out drug delivery functions. Therefore, PFOB@PLGA@Pt@DOX-CM exhibited a stronger anti-AML cell proliferation effect than PFOB@PLGA@Pt and PFOB@PLGA@Pt@CM. Fluorescence microscopy and flow cytometry were also performed to explore the anti-AML effect of nanocomposites. As shown in Fig. S2a, the green fluorescence of living cells stained with Calcein-AM kit in the PFOB@PLGA@Pt@DOX-CM group notably reduced compared with other groups. From flow cytometry results, PFOB@PLGA@Pt@DOX-CM reached the highest growth inhibition rate on AML cells, significantly reduced the viability of the cells to $22.8 \pm 4.2\%$, which was much more inhibition than PFOB@PLGA@Pt@CM and PFOB@PLGA@Pt (Fig. S2b). These results suggested that synergistic contributions of cell membranes, nanozymes, and chemotherapeutic agents promoted the killing effect of nanocomposites on AML cells.

2.8. In vivo treatment efficacy of biomimetic nanocomposites

NOD/SCID mice (18–20 g) were intravenously injected with HL-60 cells (1.0×10^6) after X-ray irradiation (250 cGy), the successful establishment of the AML mice model was verified by flow cytometry and Giemsa staining. On the 18th, 28th, and 38th day of HL-60 cells inoculation, a PE-labeled CD33 antibody was used to detect the expression of biomarker CD33 by flow cytometry to analyze the proportion of HL-60 cells in bone marrow, spleen, peripheral blood. The results showed that with increasing time HL-60 cells accounted for 7.5%, 37.1% and 92.6% in bone marrow; 2.92%, 12.4% and 56.7% in spleen; 0.71%, 3.32% and 54.7% in blood, respectively (Fig. S4). Once mice appeared AML symptoms, cells in the peripheral blood and bone marrow were collected, smeared, stained with Wright-Giemsa dye for direct observation under the microscope. HL-60 cells with large nuclei and deep blue-purple staining were shown in Fig. S3a and Fig. S3b, which proved the successful establishment of the AML mouse model.

To assess the therapeutic effect of biomimetic nanocomposites against AML *in vivo*, the AML mice were intravenously injected with normal saline, DOX, PLGA@Pt, PFOB@PLGA@Pt, PFOB@PLGA@Pt@CM, PFOB@PLGA@Pt@DOX-CM twice a week for 3 weeks at the Pt dose of 2 mg/kg and DOX dose of 1.8 mg/kg. The residual leukemic cells in the bone marrow contribute to the AML recurrence [31]. Therefore, the selective accumulation of anti-leukemia drugs in bone marrow is crucial to ensure the therapeutic efficacy of AML [32]. To investigate the accumulation ability of biomimetic nanocomposites in the bone marrow, the *in vivo* pharmacokinetics of biomimetic nanocomposites were firstly evaluated. As illustrated in Fig. 5d, there was a significant difference in blood clearance rate *in vivo* between PFOB@PLGA@Pt@DOX-CM and PFOB@PLGA@Pt. The half-life was 16.8 ± 2.6 h for the PFOB@PLGA@Pt@DOX-CM and 8.2 ± 2.3 h for the PFOB@PLGA@Pt. The half-life of PFOB@PLGA@Pt@DOX-CM was significantly longer than that of PFOB@PLGA@Pt, which could be ascribed to the stealth effect of cell membrane in blood circulation. A longer circulation of PFOB@PLGA@Pt@DOX-CM enabled biomimetic nanocomposites to efficiently eliminate AML cells in the blood and home to the bone marrow. Next, the bone marrow homing capability of PFOB@PLGA@Pt@CM labeled with Cy5.5 was tested. AML mice were intravenously injected with PFOB@PLGA@Pt@Cy5.5 and PFOB@PLGA@Pt@Cy5.5-CM at the equivalent Cy5.5 dose, leg bones were taken out for imaging after 6 h, 12 h, 24 h injection, respectively. Fluorescence signals in the bone marrow of the PFOB@PLGA@Pt@Cy5.5-CM group were significantly higher than that of the PFOB@PLGA@Pt@Cy5.5 group, suggesting that MS-5 cell membrane coating allowed for superior bone marrow accumulation (Fig. 5a). The accumulation of biomimetic nanocomposites in bone tissue was further confirmed by real-time fluorescence imaging of mice, as shown in Fig. 5c, the fluorescence intensity in the bone tissues of mice treated with PFOB@PLGA@Pt@Cy5.5-CM gradually increased with time. The quantitative results revealed that the fluorescence signals from bone marrow tissue in mice treated with the PFOB@PLGA@Pt@Cy5.5-CM were over 6.2-fold greater than the control group (Fig. S5a). In addition to the accumulation in the bone marrow, the nanocomposites also got accumulated in the liver, spleen, and lung (Fig. 5b), and the cumulative amount of the PFOB@PLGA@Pt@Cy5.5 group was greater than that of the PFOB@PLGA@Pt@Cy5.5-CM group (Fig. S5b). This is mainly due to the longer circulation time and more accumulated amount in the bone marrow of PFOB@PLGA@Pt@Cy5.5-CM compared with PFOB@PLGA@Pt@Cy5.5, resulting in the decrease of the accumulation in the viscera. Moreover, the tissue distribution of biomimetic nanocomposites *in vivo* was further confirmed by ICP-MS. It was observed that nanocomposites were mainly distributed in the liver and spleen to further metabolize (Fig. 5e). Likely, these nanocomposites could also kill AML cells transferred to the liver and spleen. These results further illustrated that PFOB@PLGA@Pt@Cy5.5-CM possesses a longer blood circulation
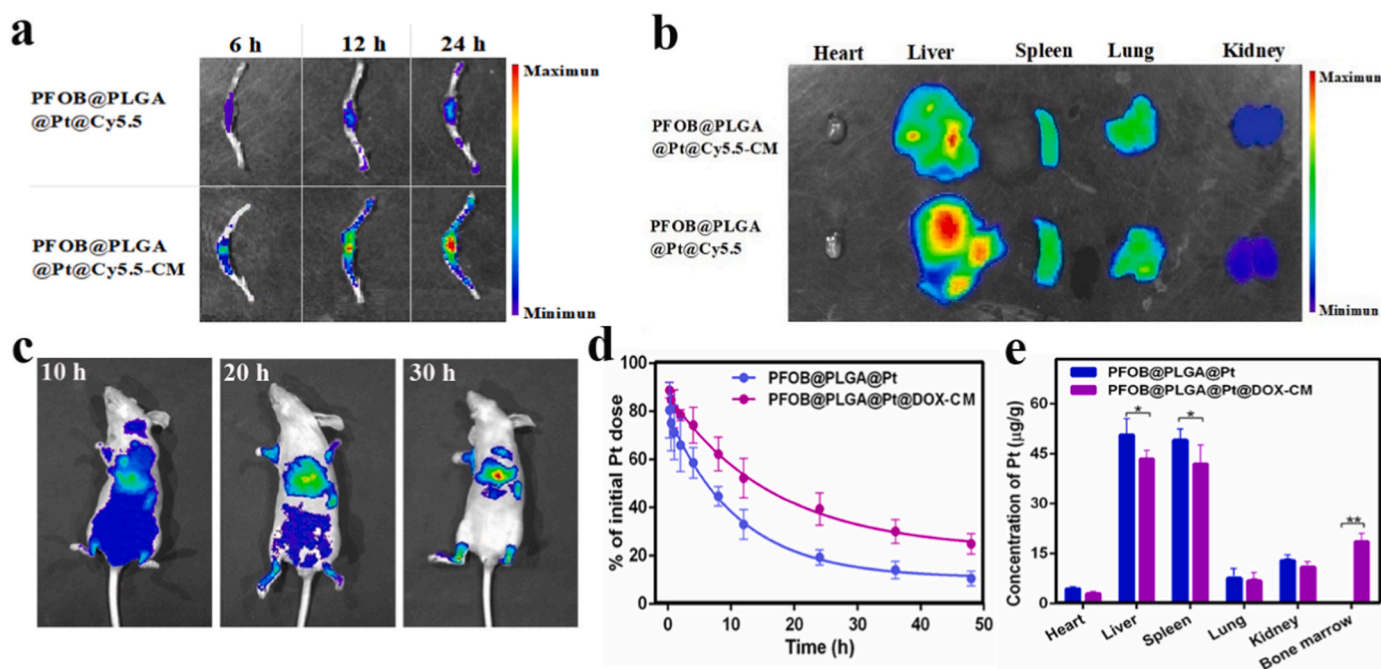
Fig. 5. Distribution and accumulation of biomimetic nanocomposites *in vivo*. (a) Fluorescence images of bone tissues from mice treated with PFOB@PL-GA@Pt@Cy5.5 and PFOB@PLGA@Pt@Cy5.5-CM. (b) *In vivo* organ distribution of PFOB@PLGA@Pt@Cy5.5 and PFOB@PLGA@Pt@Cy5.5-CM after 20 h of intravenous injection. (c) Luminescence images of mice treated with PFOB@PLGA@Pt@Cy5.5-CM for 10 h, 20 h, 30 h. (d) The blood clearance curve of intravenously injected PFOB@PLGA@Pt and PFOB@PLGA@Pt@DOX-CM at the Pt dose of 2 mg/kg (n = 4). (e) The distribution of Pt content in the main organs (heart, liver, spleen, lung and kidney) of AML mice was detected by ICP-MS after the 24 h injection of the nanocomposites.

time and can effectively accumulate into the bone marrow microenvironment.

The proportion of HL-60 cells in peripheral blood, spleen, and bone marrow was monitored by flow cytometry after three weeks of treatment. As shown in Fig. 6a, HL-60 cells in peripheral blood, spleen, and bone marrow of mice treated with PFOB@PLGA and PFOB@PLGA@Pt remarkably decreased than mice treated with saline and DOX. Importantly, PFOB@PLGA@Pt@CM was more effective in reducing HL-60 cells than either PFOB@PLGA or PFOB@PLGA@Pt. Especially, the reduction of HL-60 cells numbers in peripheral blood, spleen, and bone marrow of the PFOB@PLGA@Pt@DOX-CM group was most noticeable. By contrast, proportion of HL-60 cells in the bone marrow of the PFOB@PLGA@Pt@DOX-CM group reduced from 75.6% to 8.7%, in the spleen from 45.6% to 2.8%, and in peripheral blood from 51.6% to 2.4%, exhibiting a significant therapeutic effect on AML. The spleen is the main affected organ of AML, and splenomegaly is closely related to AML cells infiltration. Therefore, the size and weight of the spleen are considered therapeutic indicators for AML. Fig. 6d and e revealed that the spleen weight and volume of mice treated with PFOB@PLGA@Pt@DOX-CM displayed normal morphology and size while enlarged spleen was observed in other groups. The survival time was about 67 days in mice receiving PFOB@PLGA@Pt@DOX-CM. However, no mice survived beyond 61 days for treatment with PFOB@PLGA@Pt@CM, or beyond 45 days for the saline and DOX groups (Fig. 5b). Additionally, the body weight and survival time of mice were recorded throughout the treatment. As can be seen from Fig. 6c, the body weight of mice in the saline and DOX groups decreased dramatically, while the body weight of mice in the PFOB@PLGA@Pt@DOX-CM group increased slightly in comparison with other groups. In short, PFOB@PLGA@Pt@DOX-CM had the advantage of reducing the trafficking of leukemia cells to bone marrow, spleen, and peripheral blood, lending to lengthen the survival time of AML mice and reach the optimal anti-AML therapeutic efficacy.

Hematoxylin and Eosin (H&E) and CD33 proteins immunohistochemistry (IHC) staining were used to further evaluate the inhibition

effect of nanocomposites on the infiltration of AML cells into the liver and spleen (Fig. 6f). Liver and spleen in saline group occurred severe infiltration of abnormal AML cells which are characterized with darker nucleus staining, larger and irregular cell morphology. Whereas AML cells density in the spleen and liver markedly decreased after receiving treatment. Especially for the PFOB@PLGA@Pt@CM group, a small number of marked AML cells were observed. There was no obvious invasion of AML cells around blood vessels in the PFOB@PLGA@Pt@DOX-CM group. Compared with other treated groups, the histologic structure of the spleen and liver in the PFOB@PLGA@Pt@DOX-CM group was the most integrated, indicating that PFOB@PLGA@Pt@DOX-CM nanocomposites had the strongest alleviating effect on AML symptoms. A routine blood test is another important index to evaluate the AML therapeutic effect of biomimetic nanocomposites. As shown in Fig. S5c, the blood routine parameters of the PFOB@PLGA@Pt@DOX-CM group were identical to those of the healthy group, while the blood routine indexes of saline and DOX group were significantly different from those of the healthy group. WBC (white blood cell) level of mice treated with nanocomposites was lower than those in the saline and DOX group, but the HGB (hemoglobin) and PLT (blood platelet) levels tended to increase. In summary, these results showed that biomimetic nanocomposites dramatically blocked the infiltration of AML cells into the spleen and liver and reduced the systemic disease burden in mice with leukemia.

2.9. Biosafety assessment of biomimetic nanocomposites in vivo

As mentioned above, biomimetic nanocomposites have been demonstrated that have good therapeutic effects *in vivo* and *in vitro*. To further promote their therapeutic application in AML, the biosafety of biomimetic nanocomposites *in vivo* should be investigated. Firstly, the potential biological toxicity of biomimetic nanocomposites on the main organs (heart, liver, spleen, lung, and kidney) of mice was examined by H&E staining. No noticeable phenomenon of organ inflammation or injury was observed from the representative H&E staining of viscera
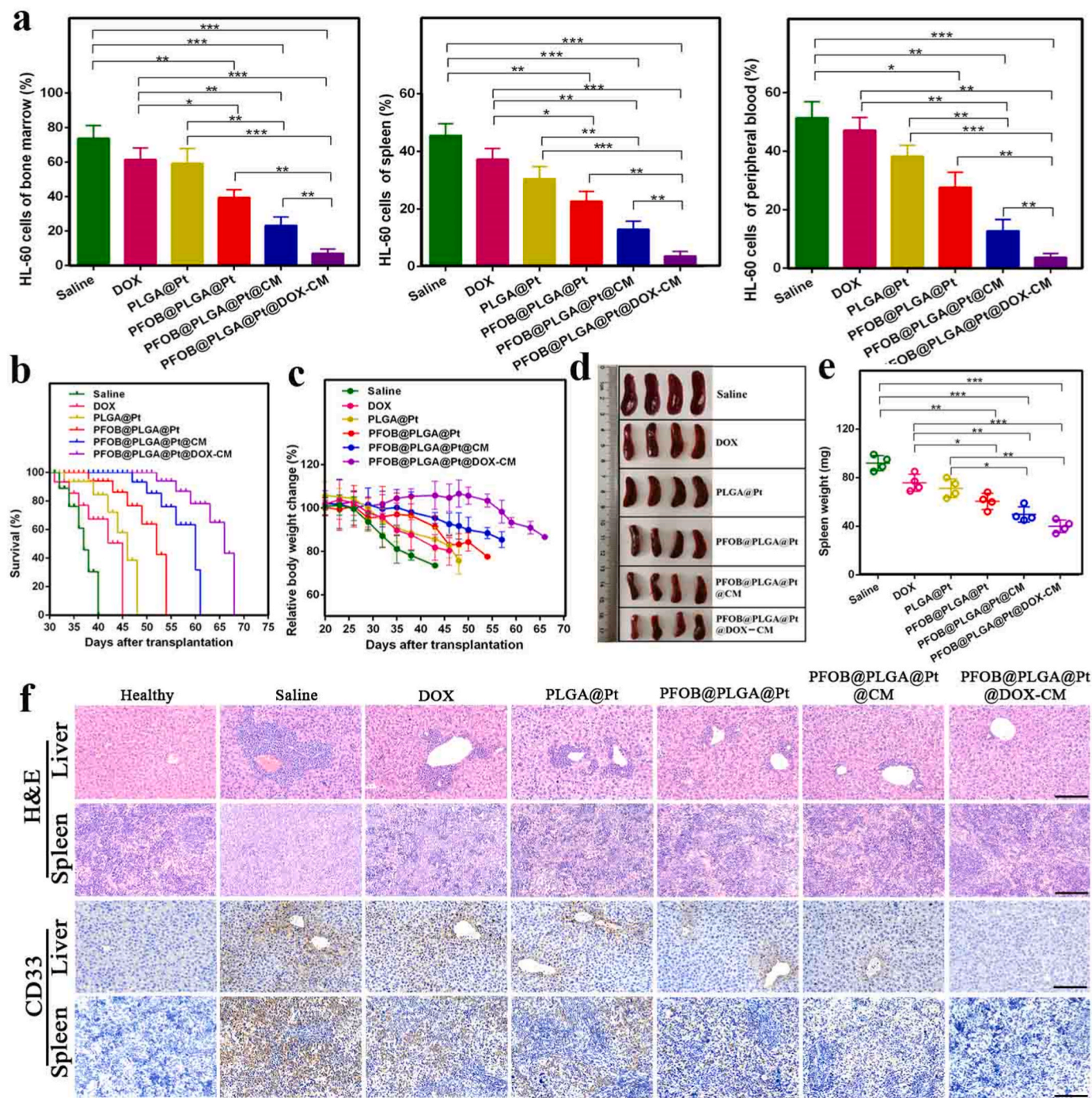
Fig. 6. Treatment efficacy of biomimetic nanocomposites *in vivo*. (a) Flow cytometry analysis of the percentage of HL-60 cells in bone marrow, spleen and peripheral blood of AML mice in each group (bars means ± S.D. *P < 0.05, **P < 0.01, ***P < 0.001, n = 4), each symbol represents an individual mouse. (b) Survival curves for treated and control mice (n = 6). (c) The relative weight change of all AML mice during treatment (n = 6). (d) Morphologies of spleens from mice received different treatments (n = 4). (e) Weights of spleens after various treatments (bars means ± S.D. *P < 0.05, **P < 0.01, ***P < 0.001, n = 4). (f) H&E and immunohistochemical analysis (CD33 positive cells) of liver and spleen to study the anti-AML infiltration effects of biomimetic nanocomposites, scale bar = 100 μm.

tissue of the treatment group and control group (Fig. 7a). In addition, serum biochemistry assays were also conducted to evaluate the biosafety of biomimetic nanocomposites on organs, especially the liver and kidney. Compared with healthy mice, the blood biochemical indexes (total protein (TP), albumin (ALB), globulin (GLO), albumin and globulin ratio (A/G), alanine aminotransferase (ALT), aspartate aminotransferase (AST), alkaline phosphatase (ALP) and urea nitrogen (BUN)) of mice injected with biomimetic nanocomposites had no significant changes, and the fluctuations were also within the normal range (Fig. 7b).

Therefore, biomimetic nanocomposites had no obvious toxicity in mice and were promising for application in AML therapy.

3. Conclusion

We presented that the biomimetic nanocomposite with enzyme-like activities and CXCR4 antagonism efficiently enhanced the therapeutic efficacy of AML. Unlike existing nanomedicine-mediated anti-AML strategies, our biomimetic nanocomposites PFOB@PLGA@Pt@DOX-CM
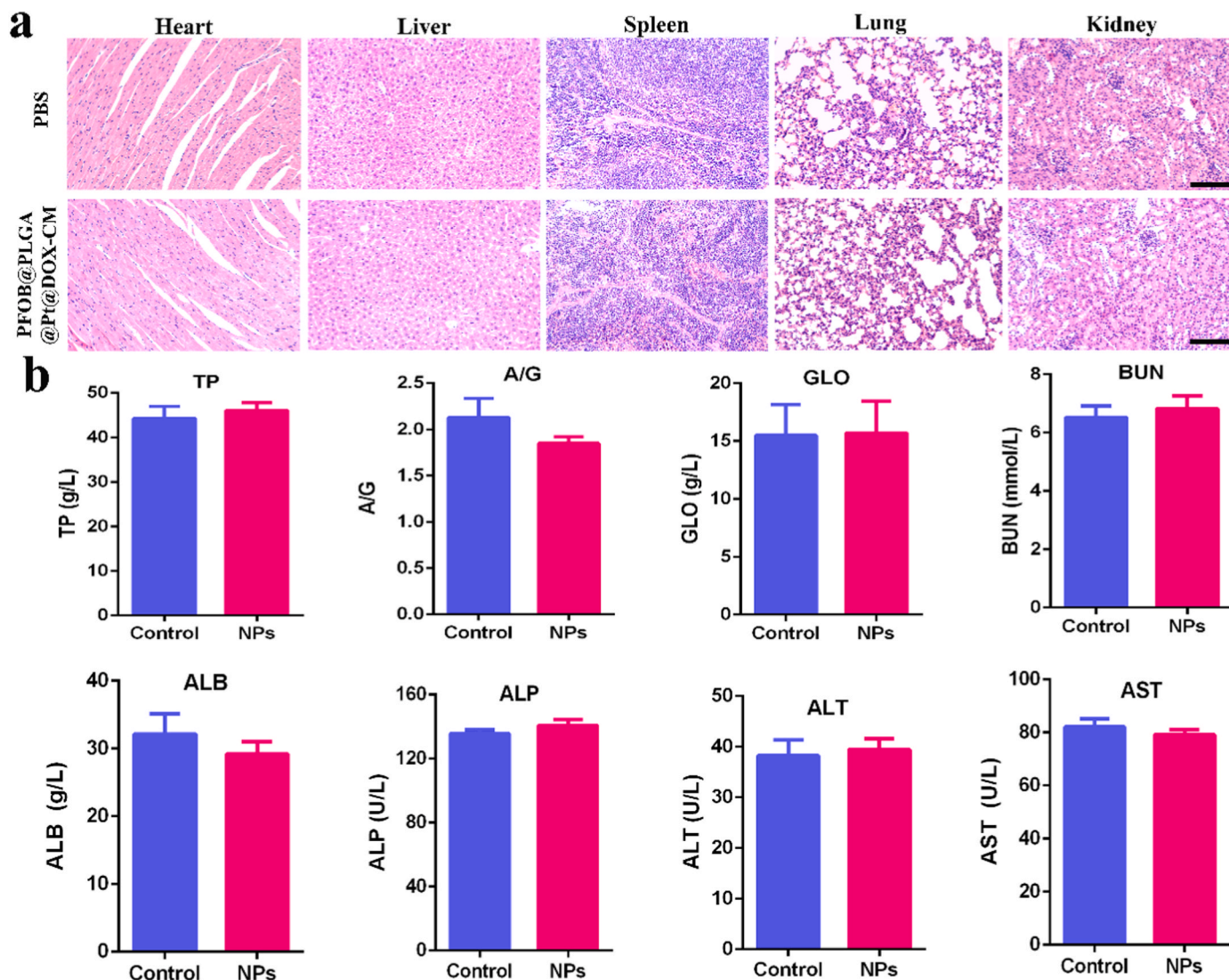
Fig. 7. Biosafety of biomimetic nanocomposites *in vivo*. (a) H&E-stained slices of the organs tissues (heart, liver, spleen, lung and kidney) from mice injected with biomimetic nanocomposites and PBS, scale bar: 100 μm. (b) Serum biochemistry (TP, A/G, GLO, BUN, ALB, ALP, ALT, AST) results were obtained from mice injected with biomimetic nanocomposites and PBS.

possess a synergistic anti-AML efficacy via integrating chemotherapy, nanozyme-induced cascade catalytic activity, and CXCR4 antagonism. In addition, these biomimetic nanocomposites PFOB@PLGA@Pt@DOX-CM could effectively home to the bone marrow and eliminate the residual leukemia cells there, at the same time, prevented infiltration of leukemia cells to the bone marrow and other organs like the liver and spleen. However, whether the biomimetic nanocomposite can overwhelm the drug resistance and relapse in AML remains to be studied. In summary, this proof-of-concept study may offer a promising approach for the treatment of AML and may improve clinical outcomes.

4. Experimental section

Synthesis of PFOB@PLGA@Pt nanocomposites: PFOB@PLGA nanoparticles were firstly synthesized by emulsifying solvent evaporation [16,33]. Briefly, 200 μL PFOB and 50 mg PLGA were dissolved in 2 mL chloroform and then were added into 10 mL 10% PVA aqueous solution for ultrasonic crushing in the ice bath (ultrasonic 2 s, stop 3 s, 40% power, 5 min). The organic reagents evaporated at room temperature by mechanical stirring (550 rpm) for 3 h to form white products of PFOB@PLGA. White products were washed three times with ultrapure water by ultrafiltration centrifugation (8000 rpm), followed by the

addition of 20 mg NH_2-PEG-SH, 10 mg EDC and continued to shake (120 rpm) for 4 h. The free PEG impurities were further removed by ultrafiltration centrifugation (8000 rpm) to obtain PFOB@PLGA@PEG-SH nanospheres. 50 mg PFOB@PLGA@PEG-SH nanospheres incubated with 15 mg H_2PtCl_6 for 12 h, and Pt^{4+} were finally reduced by 5 mg sodium borohydride to get PFOB@PLGA@Pt nanocomposites. 50 mg PFOB@PLGA@Pt nanospheres were further modified with 10 mg COOH-PEG-SH or Cy5.5-PEG-SH to obtain negatively charged PFOB@PLGA@Pt–COOH or PFOB@PLGA@Pt@Cy5.5 nanoparticles.

Preparation of PFOB@PLGA@Pt@DOX-CM nanocomposites: MS-5 cells membranes were separated by the rapid freeze-thaw method as described in the literature [34]. The MS-5 cells at the logarithmic phase were collected and rinsed 3 times using PBS. Afterward, the cells were incubated with low-osmotic PBS and were crushed by repeated freeze-thaw treatment with liquid nitrogen 8 times. Then 1 mL of 35% glucose solution was added to float the cells. The supernatant was extracted by centrifugation at a low-speed of 2000 rpm for 5 min. Next, the supernatant was discarded by high-speed centrifugation at a high speed of 12000 rpm for 10 min. Some cell organelles and inclusions were removed, cell membrane fragments were collected. 25 mg DOX or 10 mg DSPE-PEG-Cy5.5 dropped into 10 mL water solution containing the

excess MS-5 cell membranes and 50 mg PFOB@PLGA@Pt@PEG-COOH nanoparticles to vigorous stir (280 rpm) overnight. Finally, the products were centrifuged at 8000 rpm for 8 min to get rid of unloaded drugs and free cell membranes, PFOB@PLGA@Pt@DOX-CM or PFOB@PLGA@Pt@Cy5.5-CM was obtained and stored at 4 °C for future use.

Characterizations: sizes and morphologies of nanocomposites were determined by an HRTEM (JEM-2100, Japan). A particle size analyzer (ZS90, Malvern) was utilized to measure the hydrodynamic size and zeta potential of nanocomposites. Fluorescent images were acquired from CLSM (LSM700, ZEISS). Ultraviolet absorption spectra were carried out on an ultraviolet–visible spectrophotometer (Shimadzu, UV3600). Pt concentration was quantified by ICP-MS (ICPS-7510, Shimadzu). Fluorescence measurements were performed on a fluorescent spectrometer (ARL 9900, USA). Bioluminescence images were gathered with an IVIS Spectrum Imaging System (PerkinElmer). ESR detections were conducted using a Bruker EMX ESR spectrometer.

MS-5 cells, MS-5 cells membrane vesicles, and PFOB@PLGA@Pt@DOX-CM nanocomposites were homogenized in radioimmunoprecipitation assay (RIPA) buffer with 20 μg/mL protease inhibitors. The supernatant was collected after centrifugation, and the total protein content was determined by bicinchoninic acid assay (BCA assay). Later, protein denatured at 95 °C for 5 min, resolved by 12% SDS-PAGE, and transferred onto a nitrocellulose membrane for 1 h. The membrane was blocked in 5% skimmed milk for 30 min, and then incubated with primary antibodies overnight and HRP-conjugated secondary antibodies for 4 h at 4 °C. The imaging was acquired on a Bio-Rad Image Lab system.

Oxygen carrying capacity and enzyme-like activity of nanocomposites: 2 mL SO@PLGA, PFOB@PLGA, PFOB@PLGA@Pt nanocomposites (PFOB concentration of 3.5 μg/mL, Pt concentration of 14 μg/mL) aqueous solution was put into a gel volume model pipeline, respectively. The ultrasonic images were gathered with the 18 MHz probes of the high-resolution small animal ultrasonic imaging system (FUJIFILM VisualSonics Vevo 2100) to test the oxygen-carrying capacity of nanocomposites. To measure the POD-like activity of nanocomposites, 10 μL 10 mg/mL TMB substrates were catalyzed by nanocomposites (PFOB concentration of 3.5 μg/mL, Pt concentration of 14 μg/mL) in 2 mL acetate buffer solution (pH = 4.0) in the presence of H_2O_2 (32 μL, 1%). UV–vis absorption spectra of the blue TMB oxidation products were measured by an ultraviolet spectrophotometer. Michaelis-Menton kinetics measurements were performed by monitoring the change in absorbance at 652 nm of formed blue-colored products on a microplate reader (TECAN, Suisse). The effects of both TMB (0–6 mM) and H_2O_2 (0–0.5 mM) concentrations on the catalytic rate of nanocomposites were studied. Considering that glucose oxidase is easily inactivated under acidic conditions, but peroxidase activity is stronger in an acidic environment, the study of glucose oxidase activity of nanocomposites should follow a two-step method. First, the nanocomposites oxidized different concentrations of glucose under neutral conditions to produce H_2O_2, which further oxidized TMB in an acidic environment to change color, and the absorbance of TMB oxidation products was measured. In 100 μL PBS solution (pH = 7.4), the concentration of the nanocomposites was fixed (PFOB concentration of 3.5 μg/mL, Pt concentration of 14 μg/mL), 100 μL of different concentrations of glucose (1–8 mmol/L) was added, or the concentration of glucose was constant (8 mmol/L), the concentration of the nanocomposites was changed (PFOB concentration of 0–3.5 μg/mL, Pt concentration of 0–14 μg/mL), the mixed solution was incubated at 37 °C for 40 min. Then, 500 μL NaAc-HAc buffer containing 100 μL 10 mg/mL TMB (pH = 3) was added into the reaction system to incubate at 37 °C for 45 min. Finally, an ultraviolet spectrophotometer was used to measure the absorbance at 652 nm.

TA was used to monitor the production of ●OH because it can react with ●OH to produce a fluorescent product with a unique absorption peak at 435 nm. In a typical process, 1×10^{-3} M TA was placed into the reaction solution containing 0.1 M H_2O_2 and nanocomposites (PFOB concentration of 3.5 μg/mL, Pt concentration of 14 μg/mL) for 12 h, and then the fluorescence spectra of the samples were detected by fluorescence spectrophotometer. ESR measurements were also performed by ESR spectrometer at room temperature. 50 mL sample solutions containing nanocomposites (PFOB concentration of 3.5 μg/mL, Pt concentration of 14 μg/mL), 1×10^{-3} M H_2O_2, and 0.05 M DMPO were added to glass tubes and sealed. The ESR spectra were recorded 2 min after Pt-induced production of ●OH at 300 K X-band frequencies.

Drugs loading and *in vitro* release: the unencapsulated DOX in the supernatant was immediately determined with ultraviolet spectroscopy at 480 nm based on a C-A calibration curve (absorbance intensity vs concentration) to calculate the loading rate of DOX. The release behavior of Dox and Pt ions from nanocomposites was also investigated. In detail, dialysis bag of the 10 kDa molecular weight was filled with PFOB@PLGA@Pt@DOX-CM solution, and then was immersed in 200 mL PBS buffer (pH = 7.4) or NaAc-HAc (pH = 4.5) to shake at 200 rpm in the dark. 2 mL PBS buffer was taken out at predetermined times (2 h, 4 h, 6 h, 8 h, 12 h, 24 h, 36 h, 48 h, 72 h, 96 h, 120 h) and replaced with an equal volume of fresh PBS buffer. The concentration of DOX and Pt ions in the buffer solution was determined by UV spectrum and ICP-MS.

Cellular uptake of biomimetic nanocomposites: HL-60 cells (2×10^6 cells/well) were seeded in 6 well-plates and then incubated with free DOX and nanocomposites with the same DOX concentration (PFOB concentration of 3.5 μg/mL, DOX concentration of 12.6 μg/mL, Pt concentration of 14 μg/mL) for 10 h. Subsequently, some cleaned HL-60 cells were detected with flow cytometry by tracking DOX fluorescence signals to verify the cellular uptake of drugs. The other fixed cells were viewed by Bio-TEM to analyze the cellular uptake of nanocomposites, intracellular phagocytosis of nanocomposites was also quantitatively analyzed by ICP-MS.

Measurement of intracellular ROS levels: total intracellular ROS levels were measured with the Reactive Oxygen Species Assay Kit (Beyotime, China) based on the fluorescent probes of DCFH-DA. HL-60 cells were seeded in confocal microscope dishes at a density of 1×10^5 cells/well and were respectively treated with PFOB@PLGA, PFOB@PLGA@Pt, PFOB@PLGA@Pt@CM nanocomposites (PFOB concentration of 3.5 μg/mL, DOX concentration of 12.6 μg/mL, Pt concentration of 14 μg/mL) for 6 h. After treatments, cells were labeled with 5 μM DCFH-DA fluorescence probes at 37 °C for 30 min in the dark. The cells were washed three times with PBS, the fluorescence of DCF (excitation at 488 nm, emission at 530 nm) was determined with a flow cytometer (Thermofisher Scientific, Attune NxT) and a fluorescence microscope.

Cytotoxicity assay of nanocomposites: cell counting kit-8 (CCK-8) and lactate dehydrogenase (LDH) reagents were utilized to test the cytotoxicity of nanocomposites. HL-60 cells at a density of 1×10^4 cells per well were inoculated into 96-well plates for 12 h. Then the DOX, PFOB@PLGA, PLGA@Pt, PFOB@PLGA@Pt, PFOB@PLGA@Pt@DOX and PFOB@PLGA@Pt@DOX-CM with different concentrations (PFOB concentration of 1.75, 3.5, 5.25, 7 μg/mL, DOX concentration of 6.3, 12.6, 18.9, 25.2 μg/mL, Pt concentration of 7, 14, 21, 28 μg/mL) were added and continued to incubate at 37 °C for 24 or 48 h. Afterward, 10 μL CCK8 or 20 μL lactic acid was added to each well, and then absorbance at 450 nm or 490 nm was detected with a microplate reader. The relative viability of cells was calculated by comparing the experimental group and control group. The cells were stained with calcium fluorescein (AM) to intuitively observe the inhibitory effect of nanocomposites (PFOB concentration of 7 μg/mL, DOX concentration of 25.2 μg/mL, Pt concentration of 28 μg/mL) on HL-60 cells. Some cells were stained with 10 μL Annexin V-APC and 7-AAD to be checked by flow cytometry within 2 h and the obtained data were analyzed by FlowJo software.

Cell migration and adhesion assays: HL-60 cells were pretreated with PFOB@PLGA, PLGA@Pt, PFOB@PLGA@Pt, PFOB@PLGA@Pt@DOX, and PFOB@PLGA@Pt@DOX-CM (PFOB concentration of 3.5 μg/mL, DOX concentration of 12.5 μg/mL, Pt concentration of 14 μg/mL) in a

sera-free medium at 37 °C for 2 h. Then HL-60 cells (2×10^5/chamber) were seeded into the upper chambers of the transwell migration device. The bottom chambers of transwell migration equipment were dealt with 800 μL medium containing CXCL12 (100 ng/mL). After incubation for 24 h, the number of HL-60 cells migrated to the bottom chambers was collected and counted. MS-5 cells (1×10^6) were firstly seeded in a 24-well plate to construct a mesenchymal cell layer. Then HL-60 cells were labeled with 2 μM calcein-AM after pretreated with PFOB@PLGA, PLGA@Pt, PFOB@PLGA@Pt, PFOB@PLGA@Pt@DOX and PFOB@PLGA@Pt@DOX-CM (PFOB concentration of 3.5 μg/mL, DOX concentration of 12.5 μg/mL, Pt concentration of 14 μg/mL) for 2 h. Fluorescent marked HL-60 cells (1×10^6/well) were co-incubated with MS-5 cells to adhere for 2 h. The fluorescence signals (excitation light at 488 nm and emission light at 514 nm) of nonattached HL-60 cells in the upper layer were detected by enzyme plate analyzer and the relative adhesion rate of each experimental group was calculated.

AML animal model establishment: the AML mouse model was established according to the procedure described previously [35]. In brief, PBS suspension of HL-60 cells (1.0×10^6) was intravenously injected into X-irradiated (250 cGy) NOD/SCID mice (female, 18–20g, Vital River Laboratory Animal Technology Co., Ltd., Beijing). On the 18th, 28th, and 38th day of HL-60 cells inoculation, the proportion of HL-60 cells in peripheral blood, bone marrow, and spleen cells was analyzed by 2 μL PE anti-human CD33 antibody using flow cytometry. Fresh peripheral blood and bone marrow effusion were collected, smeared, stained with Wright-Giemsa, and then observed under the microscope.

In vivo therapy experiments: on the 18th day after transplantation of HL-60 cells, mice were randomly divided into six groups, which were intravenously injected with saline, DOX, PLGA@Pt, PFOB@PLGA@Pt, PFOB@PLGA@Pt@CM, PFOB@PLGA@Pt@DOX-CM at the Pt dose of 2 mg/kg (PFOB dose of 0.5 mg/kg, DOX dose of 1.8 mg/kg, in 200 μL PBS for each mouse). The injection was repeated twice a week for 3 weeks. After treatment, four mice in each group were sacrificed to collect the cells in peripheral blood, bone marrow, and spleen. The percentage of HL-60 cells in peripheral blood, bone marrow, and spleen was monitored with PE-labeled anti-human CD33 antibody (Biolegend, USA) by flow cytometry. The spleens were weighed and photographed to assess the infiltration of AML cells to the spleen at the same time. Furthermore, histopathological analysis (H&E and CD33 antibody immunohistochemical staining) on the liver and spleen was performed. The therapeutic effect of nanocomposites was also evaluated by blood routine (WBC, HGB, PLT) tests. The body weight and survival time of other mice were monitored every day. After the experimental period, partly dissected visceral tissues (heart, liver, spleen, kidney, lung) were dried, weighed, digested in aqua regia solution to quantify the distribution of Pt in the organ tissue.

Pharmacokinetics, biodistribution studies *in vivo*: for the blood pharmacokinetics study, AML mice (n = 4) were intravenously injected with PFOB@PLGA@Pt@DOX-CM or PFOB@PLGA@Pt at the same therapeutic dose. At predetermined time points (5 min, 10 min, 20 min, 30 min, 1 h, 2 h, 4 h, 8 h, and 24 h), a 10 μL blood sample was extracted from the tail to degrade in 100 μL aqua regia. Pt concentrations of these blood samples were measured by ICP-MS to calculate the blood circulating half-life of nanocomposites *in vivo*. For *in vivo* biodistribution study, the AML mice were intravenously injected with PFOB@PLGA@Pt@Cy5.5 or PFOB@PLGA@Pt@Cy5.5-CM at a Pt dose of 2 mg/kg. The leg bones (at 6 h, 12 h, 24 h of injection) and other major organs (at 24 h of injection) were taken out to record the fluorescence images using an IVIS Spectrum system. The fluorescence intensities of interest regions were quantitated by Living Image Software. The bioluminescence signals of mice were recorded at 10 h, 20 h, 30 h after injection of PFOB@PLGA@Pt@Cy5.5-CM. To correct the background bioluminescence, the signals acquired from PFOB@PLGA@Pt@Cy5.5-CM-free mice were subtracted. In addition, the *in vivo* biodistribution of nanocomposites was also evaluated by ICP-MS measurement.

Toxicity studies *in vivo*: to investigate the biosafety of biomimetic nanocomposites *in vivo*, the female BALB/c mice were randomly divided into test and control groups (n = 5). In the test group, the mice received an intravenous injection of biomimetic nanocomposites (200 μL, PFOB dose of 0.5 mg/kg, DOX dose of 1.8 mg/kg, Pt dose of 2 mg/kg) twice a week for 3 consecutive weeks, while the mice with an equal volume of PBS injection were used as the control group. Blood samples and viscera (heart, liver, spleen, lung and kidney) of mice were collected for further toxicity studies after treatment. The blood samples were pretreated to analyze biochemistry examination of liver and kidney function (TP, A/G, GLO, BUN, ALB, ALT, AST, ALP) and blood routine parameters (WBC, HGB, RBC, PLT). The viscera tissue sections were stained with H&E to observe histopathological lesions under a digital microscope.

Statistic methods. The significance of the data is analyzed according to analysis of variance: $*p < 0.05$, $**p < 0.01$, and $***p < 0.001$. The samples/animals were allocated to experimental groups and processed randomly.

Author contributions

Z.Y. proposed the idea, designed and supervised the project. K.F. completed the synthesis and characterization of all nanoparticles, as well as the verification of multi enzymatic activity and toxicity, and performed all *in vitro* and *in vivo* experiments. K.F. and B.H.Y. established AML animal models and were involved in the study of therapeutic effects *in vitro*. K.F. analyzed data and wrote the manuscript. H.H.L revised the manuscript. Y.F. provided the ultrasound imaging platform. M.M and G.N gave suggestions for the experiment.

Declaration of competing interest

I declare that the authors have no known competing financial interests、 personal relationships, or other interests that might be perceived to influence the results and/or discussion reported in this paper.

Acknowledgments

Appendix A. Supplementary data

Supplementary data to this article can be found online at https://doi.org/10.1016/j.bioactmat.2022.03.022.

References

[1] S. Abelson, G. Collord, S.W.K. Ng, O. Weissbrod, C. Hardy, K.T. Khaw, N.J. Wareham, M. Gerstung, J.E. Dick, P. Brennan, G.S. Vassiliou, L.I. Shlush, Prediction of acute myeloid leukaemia risk in healthy individuals, Nature 559 (2018) 400–404.

[2] Z.W. Li, S. W, Tumor microenvironment and drug resistance in hematologic malignancies, Blood Rev. 20 (2006) 333–342.

[3] J.W. Tyner, C.E. Tognon, D. Bottomly, B. Wilmot, S.E. Kurtz, S.L. Savage, N. Long, A.R. Schultz, E. Traer, M. Abel, Functional genomic landscape of acute myeloid leukaemia, Nature 562 (2018) 526–531.

[4] Q. Hu, W. Sun, J. Wang, H. Ruan, X. Zhang, Y. Ye, S. Shen, C. Wang, W. Lu, K. Cheng, G. Dotti, J.F. Zeidner, J. Wang, Z. Gu, Conjugation of haematopoietic stem cells and platelets decorated with anti-PD-1 antibodies augments anti-leukaemia efficacy, Nat Biomed Eng 2 (2018) 831–840.

[5] N.J. Short, M. Konopleva, T.M. Kadia, N.R. Anderson, H. Li, M.W. Harris, A. Kalinkovich, K. Golan, A. Ludin, D. Cohen, Z. Shulman, A. Avigdor, A. Nagler, O. Kollet, R. Seger, T. Lapidot, Advances in the treatment of acute myeloid leukemia:new drugs and new challenges, Cancer Discov. 10 (2020) 506–525.

[6] B. Kumar, M. Garcia, L. Weng, X. Jung, J.L. Murakami, X. Hu, Acute myeloid leukemia transforms the bone marrow niche into a leukemia-permissive microenvironment through exosome secretion, Leukemia 32 (2018) 575–587.

[7] C.C. Bleul, S. Thakur, D. Pant, Y. Zhang, E. Ju, Z. Liu, F. Cao, Z. Chen, J. Ren, X. Qu, A highly efficacious lymphocyte chemoattractant, stromal cell-derived factor 1 (SDF-1), J. Exp. Med. 184 (1996) 1101–1109.

[8] E. Tavernier-Tardy, J. Cornillon, L. Campos, P. Flandrin, A. Duval, N. Nadal, D. Guyotat, Prognostic value of CXCR4 and FAK expression in acute myelogenous leukemia, Leuk. Res. 33 (2009) 764–768.

[9] Z. Zeng, Y.X. Shi, I.J. Samudio, R.Y. Wang, X. Ling, O. Frolova, M. Levis, J.B. Rubin, R.R. Negrin, E.H. Estey, S. Konoplev, M. Andreeff, M. Konopleva, Targeting the leukemia microenvironment by CXCR4 inhibition overcomes resistance to kinase inhibitors and chemotherapy in AML, Blood 113 (2009) 6215–6224.

[10] X. Li, H. Guo, Y. Yang, J. Meng, J. Liu, C. Wang, H. Xu, A designed peptide targeting CXCR4 displays anti-acute myelocytic leukemia activity in vitro and in vivo, Sci. Rep. 4 (2014) 6610–6619.

[11] M. Mombled, L. Rodriguez, M. Avalon, P. Duchez, M. Vlaski-Lafarge, C. Debeissat, B. Perard, K.M. Sawai, J.M. Pasquet, F. Bijou, F. Thevenot, T. Cabantous, Z. Ivanovic, P. Brunet de la Grange, Characteristics of cells with engraftment capacity within CD34+ cell population upon G-CSF and Plerixafor mobilization, Leukemia 34 (2020) 3370–3381.

[12] Y. Liu, J. Luo, X. Chen, W. Liu, T. Chen, Cell membrane coating technology: a promising strategy for biomedical applications, Nano-Micro Lett. (2019) 11.

[13] Y. Wang, K. Zhang, X. Qin, T. Li, J. Qiu, T. Yin, J. Huang, S. McGinty, G. Pontrelli, J. Ren, Q. Wang, W. Wu, G. Wang, Biomimetic nanotherapies: red blood cell based core-shell structured nanocomplexes for atherosclerosis management, Adv. Sci. 6 (2019) 1900172.

[14] J. Wan, J. Wang, M. Zhou, Z. Rao, X. Ling, A cell membrane vehicle co-delivering sorafenib and doxorubicin remodel the tumor microenvironment and enhance immunotherapy by inducing immunogenic cell death in lung cancer cells, J. Mater. Chem. B 8 (2020) 7755–7765.

[15] W. Xie, W.W. Deng, M. Zan, L. Rao, G.T. Yu, D.M. Zhu, W.T. Wu, B. Chen, L.W. Ji, L. Chen, K. Liu, S.S. Guo, H.M. Huang, W.F. Zhang, X. Zhao, Y. Yuan, W. Dong, Z. J. Sun, W. Liu, Cancer cell membrane camouflaged nanoparticles to realize starvation therapy cogether with checkpoint blockades for enhancing cancer therapy, ACS Nano 13 (2019) 2849–2857.

[16] R. Yang, J. Xu, L. Xu, X. Sun, Q. Chen, Y. Zhao, R. Peng, Z. Liu, Cancer cell membrane-coated adjuvant nanoparticles with mannose modification for effective anticancer vaccination, ACS Nano 12 (2018) 5121–5129.

[17] J. Zhu, M. Zhang, D. Zheng, S. Hong, J. Feng, X.Z. Zhang, A universal approach to render nanomedicine with biological identity derived from cell membranes, Biomacromolecules 19 (2018) 2043–2052.

[18] H. Ding, Y. Cai, L. Gao, M. Liang, B. Miao, H. Wu, Y. Liu, N. Xie, A. Tang, K. Fan, X. Yan, G. Nie, Exosome-like nanozyme vesicles for H2O2-responsive catalytic photoacoustic imaging of xenograft nasopharyngeal carcinoma, Nano Lett. 19 (2019) 203–209.

[19] X. Dong, L.L. Mu, X.L. Liu, H. Zhu, S.C. Yang, X. Lai, H.J. Liu, H.Y. Feng, Q. Lu, B.B. S. Zhou, H.Z. Chen, G.Q. Chen, J.F. Lovell, D.L. Hong, C. Fang, Biomimetic, hypoxia-responsive nanoparticles overcome residual chemoresistant leukemic cells with co-Targeting of therapy-induced bone marrow niches, Adv. Funct. Mater. 30 (2020) 2000309.

[20] A. Schajnovitz, T. Itkin, G. D'Uva, A. Kalinkovich, K. Golan, A. Ludin, D. Cohen, Z. Shulman, A. Avigdor, A. Nagler, O. Kollet, R. Seger, T. Lapidot, CXCL12

secretion by bone marrow stromal cells is dependent on cell contact and mediated by connexin-43 and connexin-45 gap junctions, Nat. Immunol. 12 (2011) 391–398.

[21] N.R. Anderson, H. Li, M.W. Harris, A. Kalinkovich, K. Golan, A. Ludin, D. Cohen, Z. Shulman, A. Avigdor, A. Nagler, O. Kollet, R. Seger, T. Lapidot, CXCL12 knock-out enhances leukemia stem cell response to combination chemotherapy plus tyrosine kinase inhibition in Flt3-ITD acute myeloid leukemia, Blood 136 (2020) 7–8.

[22] T. Gu, Y. Wang, Y. Lu, L. Cheng, L. Feng, H. Zhang, X. Li, G. Han, Z. Liu, Platinum nanoparticles to enable electrodynamic therapy for effective cancer treatment, Adv. Mater. 31 (2019) 1806803.

[23] T. Gu, T. Chen, L. Cheng, X. Li, G. Han, Z. Liu, Mesoporous silica decorated with platinum nanoparticles for drug delivery and synergistic electrodynamic-chemotherapy, Nano Res. 13 (2020) 2209–2215.

[24] R. Wu, Y. Chong, G. Fang, X. Jiang, Y. Pan, C. Chen, J. Yin, C. Ge, Synthesis of Pt hollow nanodendrites with enhanced peroxidase-Like activity against bacterial infections: implication for wound healing, Adv. Funct. Mater. 28 (2018) 1801484.

[25] Y. Hao, Y. Chen, X. He, Y. Yu, R. Han, Y. Li, C. Yang, D. Hu, Z. Qian, Polymeric nanoparticles with ROS-responsive prodrug and platinum nanozyme for enhanced chemophotodynamic therapy of colon cancer, Adv. Sci. 7 (2020) 2001853.

[26] A. Dar, P. Goichberg, V. Shinder, A. Kalinkovich, O. Kollet, N. Netzer, R. Margalit, M. Zsak, A. Nagler, I. Hardan, I. Resnick, A. Rot, T. Lapidot, Chemokine receptor CXCR4-dependent internalization and resecretion of functional chemokine SDF-1 by bone marrow endothelial and stromal cells, Nat. Immunol. 6 (2005) 1038–1046.

[27] T. Wen, W. He, Y. Chong, Y. Liu, J.J. Yin, X. Wu, Exploring environment-dependent effects of Pd nanostructures on reactive oxygen species (ROS) using electron spin resonance (ESR) technique: implications for biomedical applications, Phys. Chem. Chem. Phys. : Phys. Chem. Chem. Phys. 17 (2015) 24937–24943.

[28] E. Tao, Ju Enguo, Ren Jinsong, Qu Xiaogang, Bifunctionalized mesoporous silica-supported gold nanoparticles: intrinsic oxidase and peroxidase catalytic activities for antibacterial applications, Adv. Mater. 27 (2015) 1097–1104.

[29] C. Ge, G. Fang, X. Shen, Y. Chong, W.G. Wamer, X. Gao, Z. Chai, C. Chen, J.J. Yin, Facet energy versus enzyme-like activities: the unexpected protection of palladium nanocrystals against oxidative damage, ACS Nano 10 (2016) 10436–10445.

[30] J. Kim, H. Yun, S. Kim, Human bone marrow endothelial cells elaborate non-stromal-cell-derived factor-1 (SDF-1)-dependent chemoattraction and SDF-1-dependent transmigration of haematopoietic progenitors, Br. J. Haematol. 121 (2003).

[31] L.H. Leopold, R. Willemze, The treatment of acute myeloid leukemia in first relapse: a comprehensive review of the literature, Leuk. Lymphoma 43 (2002) 1715–1727.

[32] A. Swami, M.R. Reagan, P. Basto, Y. Mishima, N. Kamaly, S. Glavey, S. Zhang, M. Moschetta, D. Seevaratnam, Y. Zhang, Engineered Nanomedicine for Myeloma and Bone Microenvironment Targeting, Proceedings of the national academy of sciences of the united states of America, 2014, p. 111.

[33] H. Wu, L. Liu, L. Song, M. Ma, N. Gu, Y. Zhang, Enhanced tumor synergistic therapy by injectable magnetic hydrogel mediated generation of hyperthermia and highly toxic reactive oxygen species, ACS Nano 13 (2019) 14013–14023.

[34] H. Xiao, S. Thakur, D. Pant, Y. Zhang, E. Ju, Z. Liu, F. Cao, Z. Chen, J. Ren, X. Qu, Red blood cell–derived nanoerythrosome for antigen delivery with enhanced cancer immunotherapy, Sci. Adv. 5 (2019).

[35] X. Li, H. Guo, H. Duan, Y. Yang, J. Meng, J. Liu, C. Wang, H. Xu, Improving chemotherapeutic efficiency in acute myeloid leukemia treatments by chemically synthesized peptide interfering with CXCR4/CXCL12 axis, Sci. Rep. 5 (2015) 16228–16239.